

Modeling of experimentally observed topological defects inside bulk polycrystals

Siddharth Singh^a, He Liu^b, Robert M. Suter^{b1}, Amit Acharya^c

^a*Department of Civil and Environmental Engineering, Carnegie Mellon University, 5000 Forbes Avenue, Pittsburgh, PA 15213 USA*

^b*Department of Physics, Carnegie Mellon University, 5000 Forbes Avenue, Pittsburgh, PA 15213 USA*

^c*Department of Civil and Environmental Engineering and Center for Nonlinear Analysis, Carnegie Mellon University, 5000 Forbes Avenue, Pittsburgh, PA 15213 USA*

Abstract

A rigorous methodology is developed for computing elastic fields generated by experimentally observed defect structures within grains in a polycrystal that has undergone tensile extension. An example application is made using a near-field High Energy X-ray Diffraction Microscope measurement of a zirconium sample that underwent 12% tensile extension from an initially well annealed state. (Sub)grain boundary features are identified with disclination line defects in them. The elastic fields of these features identified from experiment are calculated.

Keywords: Polycrystal, topological defects, high energy diffraction microscopy, elasticity

1. Introduction

The recent development of three dimensional X-ray microscopies that use unit cell orientations as the contrast mechanism [1–6] has opened up the possibility of making rigorous comparisons between observed and modeled features and responses in interior volumes of metal and ceramic polycrystalline microstructures. For example, comparisons have been made between observed plastic behaviors and model expectations including twinning [7], grain rotation and breakup [8, 9] as well as crack nucleation and propagation [10–12]. Studies of thermal responses include recrystallization [13–15] coarsening [16–19] and phase transformations leading to abnormal grain growth. [20] These studies provide direct experimental observations that can and are being used to develop improved models of materials responses. For example, experimental evidence appears to show that long held assumptions with respect to coarsening are inconsistent with observations based on X-ray microscopy. [16, 19]

Here, a demonstration is presented in which an experimentally observed topologically interesting feature is observed in the orientation field in a near-field high energy diffraction microscopy (nf-HEDM) measurements in the interior of a crystalline grain of zirconium after tensile deformation. The elastic distortion field around this feature is modeled to show the possible implication of an underlying discontinuity in the orientation field on the stress fields generated in a purely elastic medium. To our knowledge, there does not exist research efforts linking experimental measurements of orientation distributions to the possible stress fields produced by them. Restricting the discussion to the linear theory of elasticity, it is a fundamental result that smooth Nye tensor fields arising from skew symmetric tensor fields cannot produce stress. However, terminating rotation discontinuities (or discontinuities with varying magnitude of rotation jump across them) can produce stress, corresponding to distributions of disclinations and disclination dipoles in such ‘interfaces,’ the dipoles being topologically equivalent to interfacial dislocations. We leverage this idea to identify, at the scale of observations, plausible intra-granular orientation discontinuities and use (g.)disclination theory and associated computational techniques to compute their stress fields [21, 22]. Related work is [23, 24] focusing on defect kinematics where finite difference approximation are used for inferring the disclination density from observations, but no stress fields are calculated. The work [25] utilizes grain averaged elastic

Email addresses: suter@andrew.cmu.edu (Robert M. Suter^b), acharyaamit@cmu.edu (Amit Acharya^c)

strain measurements to compute intergranular elastic distortion and stress fields in a polycrystal using field dislocation mechanics theory (a subset of our equations), constraining the computed elastic strain field’s grain-wise average field to equal the measured grain average elastic strain field.

2. Experimental methods and sensitivity

High energy diffraction microscopy (HEDM) is described in detail in [6] which also summarizes a variety of applications. Here, salient aspects of the data collection procedures and the reconstruction algorithms used here for near-field HEDM (nf-HEDM) measurements are pointed out. While the data collection is time consuming and reconstructions are computationally intensive, the method outlined here is uniquely quantitative, has high dynamic range in grain size and is sensitive to subtle features as demonstrated here.

These aspects allow the mapping of small angle intra-granular orientation variations and, as a result, the identification of interesting topological features such as those of interest here.

2.1. Near-field HEDM measurement

The near-field HEDM (nf-HEDM) method is based on high resolution ($\sim 1.5 \mu\text{m}$) imaging of diffracted beams that emerge from illuminated grain cross-sections as a polycrystalline sample rotates in the line focused monochromatic X-ray beam. During rotation, each grain that is illuminated by the quasi-planar beam passes through Bragg conditions corresponding to a set of Miller indices, $\{h, k, l\}$, or, equivalently, reciprocal lattice vectors, \mathbf{G}_{hkl} . If the grains are “good” crystals (i.e., have low defect content and therefore sharp Bragg peaks), then each volume element of each grain’s cross-section satisfies Bragg conditions simultaneously (at the same values of rotation angle, ω). Each grain volume element produces a diffracted beam in the direction of the outgoing wavevector, $\mathbf{k}_f = \mathbf{k}_i + \mathbf{G}_{hkl}$, with \mathbf{k}_i being the incident beam wavevector. These parallel beams generate anisotropically projected images of horizontal grain cross-sections on a two dimensional detector oriented perpendicular to the incident beam. Diffracted beam images are collected as the sample rotates through contiguous intervals of width $\delta\omega$ as the sample rotates through a total range $\Delta\omega = 180^\circ$. To encode the directions of each scattered beam, measurements are done at two rotation axis-to-detector distances, L_1 and L_2 . The sets of projected images from each grain allow information about grain shapes and the crystal unit cell orientations to be deduced by reconstruction software.

If grains have substantial defect content and are therefore not “good” crystals, they may have orientation gradients which will spread diffracted beams over arcs on the detector images and over multiple neighboring images. In cases where grains break up into discrete blocks, for example due to deformation via single slip, the above description still holds if we re-define what we mean by a “grain:” a grain becomes any region in the sample over which the unit cell orientation is uniform on the scale of the orientation resolution of the measurement. Continuous lattice bending can lead to intensity patterns in which individual pixels receive contributions from sample regions with different orientations; such patterns become difficult to quantitatively interpret. A further complication arises from the fact that the intensity striking a given pixel arises from a sample volume determined by the scattering geometry specified by the orientation of \mathbf{k}_f and the scattering angle conventionally referred to as 2θ , with θ being the Bragg angle; both quantities are specified by the orientation and magnitude of \mathbf{G}_{hkl} for each Bragg peak.

The above procedure yields a set of $N = 2 \Delta\omega/\delta\omega$ detector images that encode a two dimensional unit cell orientation field in the illuminated layer that generated them. Full three dimensional information is obtained by measuring successive layers as the sample is translated normal to the plane defined by the line focused incident x-ray beam. Since x-rays are non-destructive in hard materials (metals, ceramics, minerals), successive measurements can be carried out between processing steps that alter the microstructure to reveal heterogeneous responses. For example, evolution under heat treatments [14, 16–18, 26] and mechanical loading [7–9, 27] have been carried out using this near-field method. [6]

2.2. NF-HEDM Reconstructions: sensitivity to intragranular lattice rotations

Converting a measured set of diffraction images into a discretized map of the microstructure that produced them is referred to as a reconstruction. For the present, the “microstructure” refers only to the field of unit cell orientations (additional quantities such as material density, phase, [20] composition, and elastic strain state [28] can be added) and the output is frequently referred to as a “grain map.” Assuming the line focused

x-ray beam has a thickness well below the grain size, the approximation is made that the cross-section is a two dimensional plane through the sample. A sample coordinate system [4] is defined as having its z_s -axis perpendicular to the plane of the x-ray beam (typically vertical in the laboratory); the x_s and y_s axes are both defined as perpendicular to z_s and parallel and perpendicular to \mathbf{k}_i , respectively, *when the rotation angle* $\omega = 0$; these axes are defined to form a right handed coordinate system. The origin of z_s is chosen arbitrarily and x_s, y_s origins are defined to be at the rotation axis. Note that many other conventions are used in various laboratories and in other software packages.

The Python-GPU based HEXOMAP package [29] is used to perform reconstructions. The code uses a C++ library of routines that were written for the well exercised and verified [30] previous generation code. [5] Preliminary image analysis routines extract signal from background in the diffraction images as described in [31]. HEXOMAP optimizes orientations on a square array of points in the illuminated sample space. It is straightforward to import three dimensional sets of these arrays into a variety of analysis and materials simulation codes. Orientations are reported as $R(\mathbf{r}_s)$ where R represents an active rotation that takes the reference unit cell orientation and rotates it into the orientation determined at sample position, \mathbf{r}_s .

A brief summary of the orientation optimization process will help to justify the sensitivity to intra-granular features that is used here. Given the experimental geometry and a trial unit cell orientation at a particular sample point or voxel position, \mathbf{r}_s (in the illuminated plane at z_s), the software determines the value of ω at which each Bragg peak will occur, computes the laboratory position of the sample point at that ω , and projects the diffracted beam from that position, along \mathbf{k}_f , and onto the detectors. If the diffracted beam strikes detector pixels that contain intensity in the experimental measurement, then an overlap counter is incremented. A confidence or completeness metric, \mathcal{C} , is computed as the ratio of the number of peaks that overlap experimental signal to the total number of simulated peaks that strike the detectors. The optimization routine performs a hierarchical search over a symmetry reduced fundamental zone of possible orientations and reports back the orientation that maximizes \mathcal{C} . The orientation in each voxel undergoes a final local Monte Carlo optimization that removes any discreteness due to the orientation mesh.

In the nf-HEDM geometry, over the $\Delta\omega = 180^\circ$ rotation range, and for arbitrary unit cell orientations, R , typical elemental metallic crystals generate 50 to over 100 Bragg peaks that strike detectors. The optimal R for each voxel puts each of its peaks into the correct sample rotation interval of width $\delta\omega$ and makes each peak overlap experimentally observed spots within those images (with two detector placements measuring the same intervals, the simulation must overlap experiment at both detector positions). The orientation is highly constrained. Empirically, using $\delta\omega = 1^\circ$ results in orientation noise within “perfect” crystals of $\leq 0.1^\circ$. [30] Rotations through angles well below $\delta\omega$ will move a subset of peaks that occur near the edges of the orientation bins into neighboring intervals. Thus, even small unit cell rotations deep within grains (where projections should land in the interiors of experimental spots) can shift intensity to independently measured images.

The computationally intensive procedure outlined above combined with relatively slow layer-by-layer data collection makes these quantitative measurements significantly more expensive than other grain mapping methods that resolve intra-granular properties. [32, 33] However, the 2D-to-2D projection of sample cross-sections to area detectors makes feature signals transparently accessible (rather than having to be extracted from intensity profiles) and the voxel-by-voxel reconstruction assumes only local, micron scale crystallinity. In this paper, we take advantage of these aspects of nf-HEDM and HEXOMAP to resolve interesting internal defect structures within the grains of an *in situ* deformed zirconium polycrystal.

2.3. Measurement of tensile deformation of zirconium

The data set that is investigated here is reported in [7, 34]. Detector images span $\delta\omega = 1^\circ$ integration intervals. A custom built loading system that is compatible with the near-field experimental geometry applies tensile load under displacement control with a load cell reading the applied force. The nf-HEDM measurement includes data from 50 layers separated by 4 μm in z_s in each of four extension states, denoted S0 through S3. The focus here is on states S0, the pristine annealed state with well ordered grains and state S2 in which tensile extension of 13.6 % has been applied.

The original analysis, using IceNine reconstructions, [5] focuses on deformation twinning observations [7] that run counter to expectations based on the sample’s “clock” texture with c -axes predominantly almost perpendicular to the loading axis. An example of pyramidal slip induced lattice rotations (which are favored by the texture) is also observed. [34] The sample’s cross-sectional area evolved anisotropically, again due

to texture. The c -axes of grains are not only preferentially oriented far from the loading axis, they are also clustered in the perpendicular plane. In S0, the average cross-section dimension is $883 \mu\text{m}$ and in S2 it is $825 \mu\text{m}$.

The results reported here are based on HEXPOMAP reconstructions of states S0 and S2 using the original raw experimental image data. The reconstructions are qualitatively similar to those in [7]; quantitative comparisons cannot be carried out since the older reconstruction output files were lost in a disk crash. Each layer reconstruction was performed at sample points on $1.48 \mu\text{m} \times 1.48 \mu\text{m}$ meshes spanning the sample cross-section dimensions. Because the detector pixel pitch is $1.48 \mu\text{m}$, this mesh is at the measurement resolution of individual diffraction images.

3. Experimental observations

Figure 1 shows a single cross-section through the zirconium sample’s microstructure in the S0 and S2 states. The cross-section shown is in the center of the measured volume. In S0, this is measured layer number 25 of 50. In S2, it is layer 27. In both cases, only voxels with $\mathcal{C} > 0.4$ are plotted; in (a), virtually all voxels are included while in (b), black areas have $\mathcal{C} < 0.4$, an indication of severe deformation or substantial elastic strain. Also in both cases, black lines are drawn between all neighboring reconstructed points that have orientations that differ by a rotation angle greater than 1.1° . In (a), only well defined grains are delineated, indicating low orientation disorder and defect content, whereas in (b) grain boundaries are still observed, but substantial intra-granular misorientations also appear. Many grains that appear in (a) remain in (b) but in most cases are deformed as well as having internal orientation discontinuities. The light green grain towards the upper right with the black line extending through most of the cross-section is the subject of the analysis below (see Fig. 5).

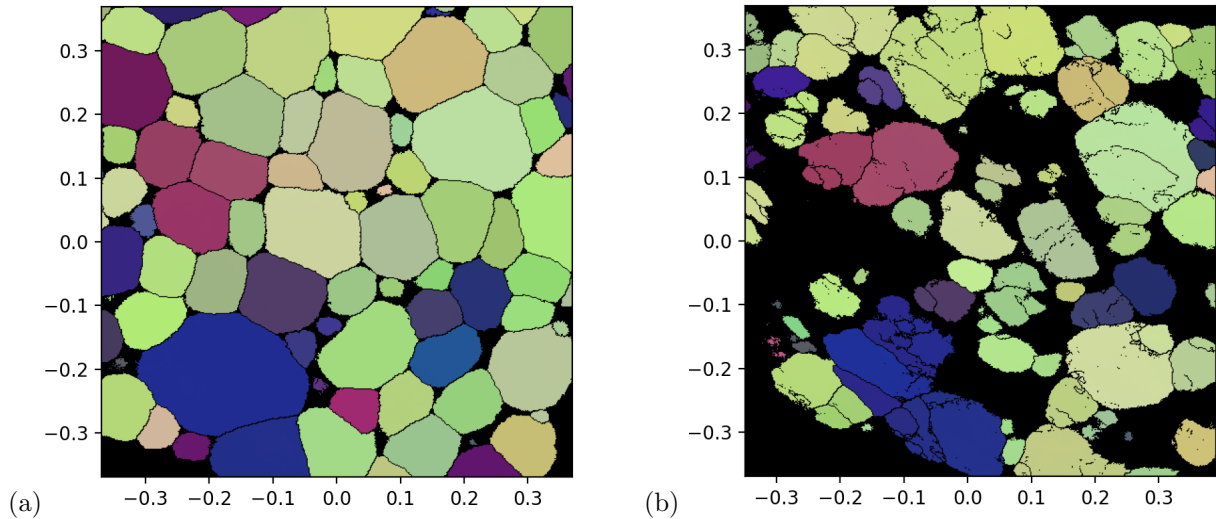


Figure 1: Corresponding cross-sections through the microstructure in (a) S0 and (b) S2 states. Axis units are in millimeters and colors are mapped from the three parameters specifying unit cell orientations (Rodrigues vector components).

Figure 2 shows the extracted grain of interest with black boundary lines drawn for different thresholds. (a) shows that the orientation in the grain is relatively uniform (as does the apparent color) but, by looking at a lower threshold in (b), additional internal structure is observed. An apparent orientation discontinuity is seen extending across the lower left quadrant while a similar feature is seen near the top. We focus here on the more extended lower feature in the analysis below.

4. Modeling of the observed orientation field

Our goal here is to estimate the linear elastic stress fields of (low angle) grain boundaries, identified from HEDM data. Our calculations are sensitive to longitudinal variations, along the boundary, of the rotation

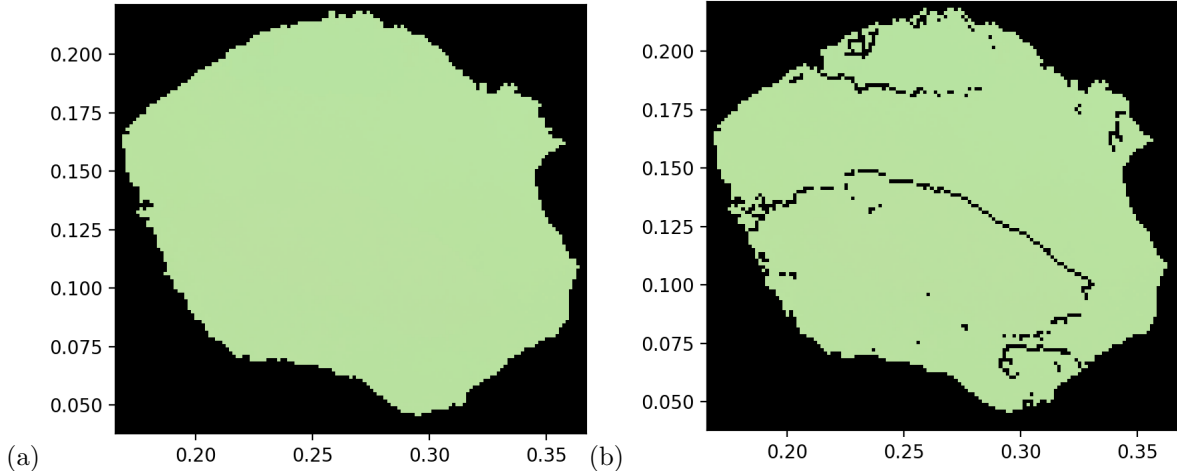


Figure 2: The grain cross-section chosen for analysis. In (a) the threshold for drawing a black line between voxel points is 5° whereas in (b) the threshold is 1.1° .

jump across the boundary (obviously measured at some finite resolution). An extreme case of such a variation is if the boundary terminates - such a terminating line is a disclination line. Similarly, smaller less extreme variations along the boundary form a continuous distribution of disclination density, contained within the boundary. Disclination dipoles are topologically equivalent to a dislocation. Individual disclinations store high levels of elastic energy in the far-field and for this reason usually appear in dipole combinations in boundaries. A series of such disclination dipoles are an alternate picture of the structure of a low-angle boundary comprising a dislocation wall.

Based on the measurements, we say that an (s)gb lies in the jagged curve formed by the voxel boundaries, see Fig. 3. However, we attribute a smooth shape and a normal to that interface by connecting the voxel

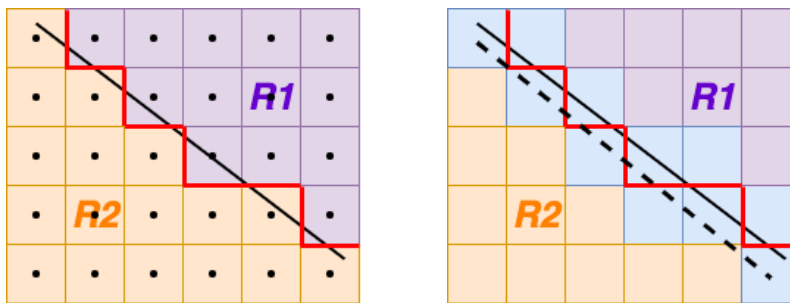


Figure 3: Outline of (s)gb identification for computations: Left panel - Two different rotation fields are shown on either side of an actual (s)gb (solid black line). The stepped red line represents an (s)gb as identified by the measurement. Right panel - For modeling, we identify boxes (marked as blue) across which there exists large rotation gradients. We obtain the (s)gb by passing a smooth curve (dashed black line) through the centers of some of those voxels.

centers abutting it which correspond to regions of high gradients in measured orientations (described by the magnitude of the field P subsequently defined in (5)). The smoothed interface so defined is assumed to be the surface/curve across which the orientation jumps (at the scale of observations). This is the best that can be done with the available information. In this interpretation of the data, no orientation (or distortion) can be assigned to the interface - and the tangential gradient of orientation/distortion is assumed to vanish at the interface. Thus, the only measurement attributable to the interface is an assertion of the normal gradient of orientation across it, given by the jump in orientation/distortion, divided by the width of the boundary, an input to the theory. This normal gradient field constitutes the eigenwall field, S , of the theory defined in Sec. 4.1. The theory suggests that any region of the interface where the orientation/distortion jump varies longitudinally along it serves as a source for stress (a location of non-zero Π field). For example,

in a twin boundary with curvature, this must be true as the distortion jump depends on the normal. We note that a tangential variation, of the jump in orientation normal to the interface, is not related in any way to assigning orientations to the interface, or a tangential gradient of the orientation field on the interface. In our calculations, we will be conservative and assign the width of the boundary to be a voxel length, having the effect of predicting lower stresses due to the identified defects. The calculations in this paper involve linear pde, so this amounts to a scaling of stress fields by a constant factor.

4.1. Elements of g.disclination theory

We review here the static elastic g.disclination theory of [21, 22].

The (inverse) elastic distortion and the eigenwall fields are the main kinematic ingredients of the model. Unlike interfaces of (inverse) displacement discontinuity which may or may not be physically identifiable (e.g., identifiable stacking faults, or ‘perfect’ 1-atom spacing shifts across an atomic layer otherwise), (inverse) elastic distortion discontinuities (at a macroscopic scale) are always identifiable. If W denotes the (inverse) elastic distortion, at an interface like a phase or grain boundary it has a large gradient over a thin interfacial region; we think of this concentrated gradient as the ‘singular part’ of W and refer to it as the *eigenwall* field $-S$. The singular part is separated out of the (distributional) derivative of W , DW to define the ‘regular part’ of DW as

$$Y := DW - (-S) = DW + S. \quad (1)$$

Y, DW, S are third order tensor fields.

When the elastic distortion U^e is small, $W \approx I - U^e$, in which case (1) can be expressed as

$$Y = -DU^e + S.$$

With X as the alternating tensor and the *definition* $Y : X =: \alpha$

$$Y : X - S : X = \text{curl } U^e \quad \implies \quad \alpha + (-S : X) = \text{curl } U^e. \quad (2)$$

Since both terms on the l.h.s. of (2) are sources of incompatibility of the elastic distortion (since $\text{curl } U^e = 0$ implies that U^e is a gradient in simply connected domains), (2), along with the physical interpretation of the eigenwall field, says that $-S : X$ is the *interfacial dislocation density* and α is the *bulk dislocation density* field. *Both serve as sources for elastic distortion* of the body causing stress (in many, but not all, circumstances).

Another important source of elastic distortion is the *g.disclination density* Π defined as

$$\text{curl } Y = \text{curl } S =: \Pi.$$

In the following we define Ω as the domain of interest in which we want to calculate elastic distortion fields and stress due to interfacial dislocation density fields (and possibly bulk dislocation density fields). As explained in [22], in order to deal with stress fields arising from longitudinal gradients of the eigenwall field along grain and compatible phase boundaries, i.e., g.disclination density fields, we define

$$\begin{aligned} \text{curl } S^\perp &= \text{curl } S && \text{on } \Omega \\ \text{div } S^\perp &= 0 && \text{on } \Omega \\ S^\perp n &= 0 && \text{on } \partial\Omega \\ \text{div } DH &= \text{div } S && \text{on } \Omega \\ (DH)n &= Sn && \text{on } \partial\Omega. \end{aligned}$$

so that

$$S = S^\perp + DH.$$

Then, with the definition $\hat{U}^e := U^e - H$, (1) may be equivalently stated as

$$Y - S^\perp = -D\hat{U}^e \quad (3)$$

so that

$$\alpha - S^\perp : X = \text{curl}(U^e - H) =: \text{curl } \hat{U}^e.$$

Finally, defining the constitutive equation for stress to be $\sigma = \mathbb{C} \hat{U}^e$, where \mathbb{C} is the tensor of (possibly anisotropic) linear elastic moduli, the elastostatic field equations at ‘small distortions’ become

$$\begin{aligned} \alpha - S^\perp : X &= \text{curl } \hat{U}^e \\ \text{div}(\mathbb{C} \hat{U}^e) &= 0 \quad \text{on } \Omega \\ (\mathbb{C} \hat{U}^e)n &= t \quad \text{on } \partial\Omega, \end{aligned} \tag{4}$$

where t is a statically admissible applied traction field (possibly vanishing).

The lhs of (4) shows the sources of elastic distortion. It can be shown [22, Sec. 6] that when S is skew in its first two indices (as happens with the modeling of low angle (sub) grain boundaries, as is the case here) the elastic strain and stress depend only on the knowledge of the bulk dislocation density α and the (g.)disclination density Π . It can also be inferred that, under the same assumption, if S^\perp is replaced by S and \hat{U}^e by U^e in (4), then $\hat{U}_{sym}^e = U_{sym}^e$ and the stress and elastic strain remain unchanged. However, the rotation fields $\hat{U}_{skw}^e \neq U_{skw}^e$, if $S \neq S^\perp$.

4.2. Definition of the input to the computational model

In this first demonstration, we will restrict ourselves to calculations of elastic fields that vary only in 2 dimensions. This requires the definition of observed rotations with axis of rotation perpendicular to the plane of field variations. In the following, we describe the procedure for defining this input.

We note that the above restriction is simply for simplicity in this work - our theory and experimental techniques are appropriate for 3-d analysis and finite deformation elastic field analysis.

After reconstruction, we have an orientation/rotation field in the whole 3-d domain. The domain comprises a collection of contiguous voxels, spatial regions of size $1.48 \mu\text{m} \times 1.48 \mu\text{m}$ as discussed in Sec. 2.3. We focus our attention on the rotation field in a particular 2-d layer; specifically, the planar section of the sample shown in Fig. 2. This section is defined by the experimental geometry as one of the 50 measured planes illuminated (successively) by the X-ray beam; these planes are perpendicular to the tensile axis and most grains have their c -axes lying close to this plane. This geometry favors the occurrence of prismatic slip events which result in lattice rotations about axes close to the c -axis. [34] We then choose the grain which contains the internal feature of interest.

The theory works with the inverse elastic distortion tensor, W , and we assume that discontinuities in inverse elastic distortion occur only through its rotation field. Thus, we focus on the measured orientation field whose transpose gives the rotation of the inverse elastic distortion. As mentioned, the study by Lind et al. [34] indicates that sections perpendicular to the tensile axis (the sample z -axis) are candidates for planes which are expected to be intersected by interfaces of rotation discontinuity.

Our experimental data processing confirms this expectation for one such plane, as shown in Fig. 5. To convert the 3×3 matrix data on this plane for our 2-d analysis, we retain the upper-left 2×2 sub-matrix of the 3×3 transpose of the rotation matrix written in the sample basis. The distortion field so obtained is not a pure rotation field, but this is not an impediment for our elastic field calculations as it can treat full distortion discontinuities and not just rotational ones.

With the 2-d distortion field in hand, we define a field P which is a discrete gradient of the (inverse) elastic distortion field. It captures the idea of how the (inverse) elastic deformation field varies in all directions. The value of the field P in the gray voxel in 4 is calculated from the difference in the 2-d distortion field values in the blue voxels in 4, in two orthogonal directions. Equation (5) gives the definition:

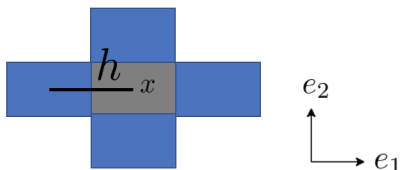


Figure 4: Calculating P field for the gray voxel using distortion data available on the blue voxels

$$DR_i(x) = R(x + he_i) - R(x - he_i)$$

$$P = \sum_{i=1}^2 DR_i \otimes e_i \quad (5)$$

The field P contains information about the discontinuity in the (inverse) elastic field at the voxel level. With the understanding that along (s)gbs the magnitude of orientation discontinuity is relatively high (above the noise level present in the experiment), we set a threshold significantly above the noise level to extract voxels with values of $|P| = \sqrt{P_{ijk}P_{ijk}}$ above the threshold. These voxels are then used to define (s)gbs.

As evident from the Fig. (5), we are able to identify at least 2 interesting features. One is a low-angle grain boundary(sub-grain boundary) and the other is a feature in which, at a given threshold, the discontinuity in the (inverse) elastic field ends within the body. As already explained, given a candidate (s)gb shape identified by the $|P|$ -above-threshold voxels, we next calculate the value of the distortion jump, or eigenwall field S , to be assigned to such voxels.

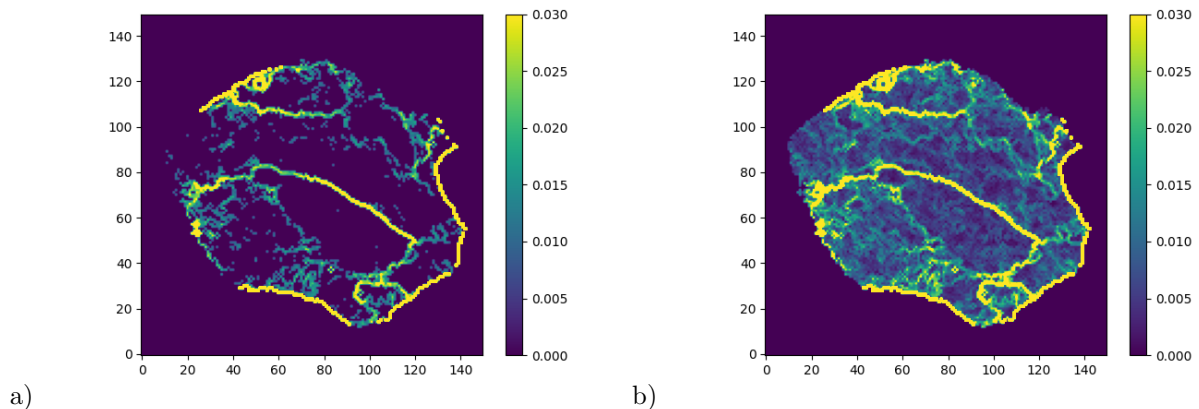


Figure 5: Voxels on the yellow zone of the colormap are having more jump in distortion field. In a) $|P|$ for reduced 2D (inverse) elastic distortion field is plotted b) $|P|$ is of full 3D rotation field. Scale: 1unit = $1.48 \mu\text{m}$

4.2.1. Construction of the eigenwall field S from experimental data

The eigenwall field S takes third-order tensors as field values and provides a discrete directional derivative of the orientation, in the direction of the normal n to the (s)gb. This normal, n , is not constant for the curve (in this 2-d situation) as evident from the shape of the features. It is evaluated by performing a cross product of the tangent vector along the (s)gb (formed at any voxel center by joining it to the next center in the (s)gb) with the unit vector perpendicular to the plane of the paper, and then normalizing it to make it unit vector. The S field is then extracted by evaluating the normal ‘action’ of P on n as follows.

$$S = \frac{1}{h}(Pn) \otimes n. \quad (6)$$

We note that along an (s)gb identified by the $|P|$ field, not all voxels are necessarily “lighted up” by a non-zero value of the S field.

4.3. Simulations and results

The left panel in Fig. 6 represents a grain delineated by a grain boundary with an sgb within it as identified from our experimental data. The gb and sgb have prescribed eigenwall fields on them (in fact the entire domain has prescribed eigenwall field on it), processed from experimental data as described above. As this grain belongs to polycrystal assembly, for the purpose of getting an idea of the stress field in the grain, we embed the isolate grain within a larger elastic domain with the same elastic properties and perform simulations of the theory in Sec. 4.1. The right panel in Fig. 6 shows this larger domain. We solve the stress equilibrium and elastic incompatibility equations, system (4), with zero-traction boundary conditions.

Solutions for the elastic distortion is known to be unique up to constant skew tensor, and this is assigned arbitrarily for the purpose of stress field evaluation. If the distortion field is to be recovered, the known value of the experimental orientation field can be specified at one point of the domain.

An important characteristic of our computational methodology based on weak formulations of the governing equation (4) implemented by adapted algorithms within the Finite element method is that we do not have to calculate any derivatives of the S field for the stress analysis, even though the calculations faithfully represent the stress field of the (g.)disclination field Π .

For the calculations described below, a domain size of 150×150 voxels is used; each voxel is a square of edge length $1.8\mu\text{m}$.

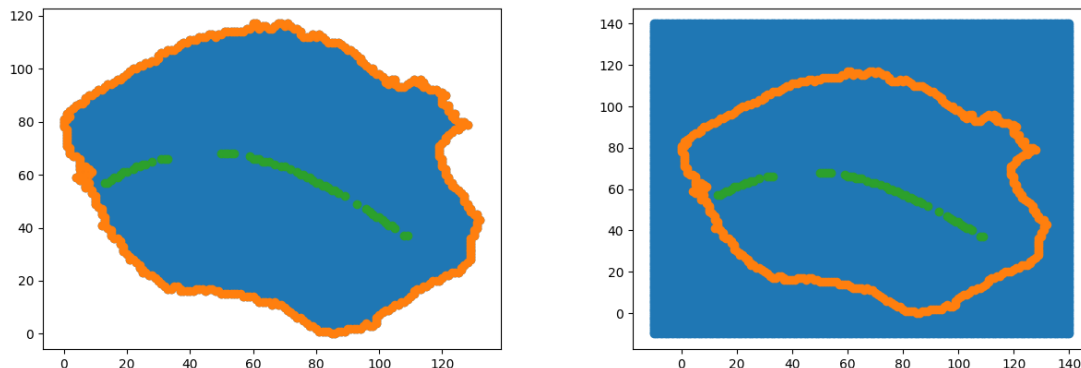


Figure 6: Left: Grain delineated by a grain boundary with an sgb. Right: The simulation domain obtained after padding the grain. Here, green shows the sub-grain boundary, orange shows the grain boundary and blue shows the elastic domain

We simulate two different cases:

- the domain with only the sub-grain boundary (SGB);
- the domain with both the sub-grain and the grain boundary (SGB+GB).

In each case, we find that stress field has high magnitude in the region where the S field varies along the interface, especially at terminations. The stress field on average is stronger in the SGB+GB case compared to the SGB case.

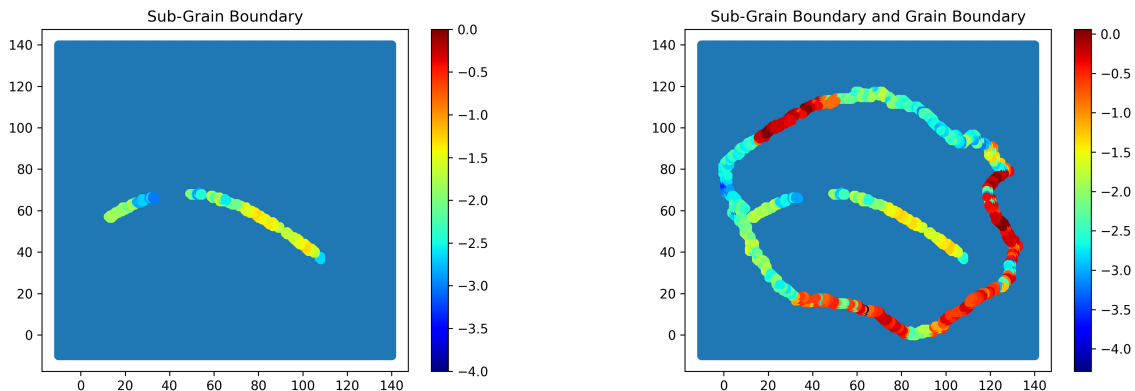


Figure 7: $\log|S|$ is plotted in the domain for two simulated cases, red color corresponds to high value of jump in distortion field

The high magnitude of stress field due to grain boundary (high-angle grain boundary) is evident from Fig. 8 that the pattern along the SGB in the first simulation has diluted in the SGB+GB case.

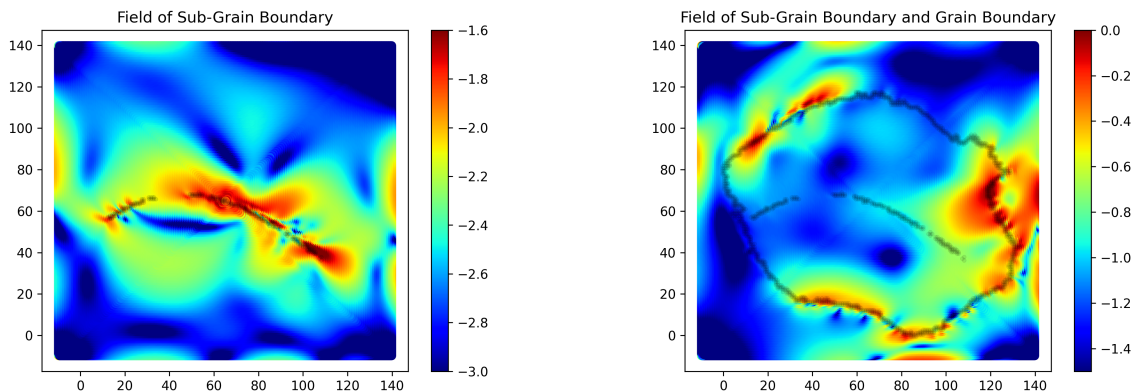


Figure 8: $\log|T|$ is plotted for two simulated cases. Stress field is normalized w.r.t shear modulus

The region of low stress magnitude (blue region just below the SGB) in the SGB case has increased in magnitude by order of approximately 2 in the SGB+GB case. This observation is evident about the non-local nature of these stress-fields. These stress fields also extend to the boundaries of the domain in both cases.

These interfaces produce stresses that are sufficient to induce plasticity.

5. Discussion

An HEDM measured dataset has been analyzed to isolate (s)gb features based on discontinuities (at the scale of observation) in the orientation field. These features have then been used to calculate their elastic fields. Sources for the elastic fields arise from longitudinal variations of the rotation jump across the boundary, specified from the analysis of the experimental data.

Limitations in calculating the exact shape of the feature arise from the disparity in (s)gb thicknesses and the resolution of the observations. Further limitations of translating available experimental data to input for elastic field calculations lies in the manual intervention required in determining an (s)gb manifold (in this work, e.g., the calculation of the tangent along a best approximated (s)gb curve).

The calculations of defect elastic fields have been restricted to 2-d, small deformation, linear, isotropic elasticity. Computational capability for 2-d, finite deformation anisotropic elastic calculations of g.disclination defect fields is available to us [22]. As well, finite strain, dislocation plasticity codes in 2 and 3-d have also been developed by us [35–37]. While theory and algorithms for 3-d, g.disclination based elastic field calculations have been developed by us [22], a computational implementation for 3-d calculations needs to be developed. Finally, dislocation plasticity calculations in 3-d are computationally expensive, and more efficient strategies for parallel computation are needed to realize the potential of our combined experimental-theoretical advances.

6. Conclusion

This proof-of-principle calculation demonstrates a method that takes advantage of spatially resolved experimental measurements of unit cell orientation fields in three dimensions. The measurements include intra-granular orientation variations as well as rotations that naturally occur at grain boundaries. Future work will also include the evaluation of inhomogeneous strain fields within grains [28]. One example of a topologically interesting unit cell orientation discontinuity has been analyzed here. Future work will extend the calculations to three dimensions and apply the methodology to cases where multiple orientation discontinuities occur within a single grain. A grand and glorious goal is to use the full power of our mesoscale field dislocation mechanics [35–37] to model sample evolution from the S0 state to S2 of Fig. 1 and/or analogous evolution in other materials. Such exercises will help shed light on the prediction capabilities of our theoretical-computational models leading to their further refinement, as well as raise interesting

questions for extending experimental measurements to more incremental sequences of states and to the use of complimentary techniques with higher spatial resolution in nanoscale grains in small samples [38].

Acknowledgments

This work was supported by the grant NSF OIA-DMR #2021019.

References

- [1] H. Poulsen, *Three-Dimensional X-ray Diffraction Microscopy*, volume 205, Springer Tracts in Modern Physics, Berlin, 2004.
- [2] W. Ludwig, P. Reischig, A. King, M. Herbig, E. Lauridsen, G. Johnson, T. J. Marrow, J. Y. Buffière, Three-dimensional grain mapping by x-ray diffraction contrast tomography and the use of friedel pairs in diffraction data analysis, *Review of Scientific Instruments* 80 (2009) 033905.
- [3] A. King, M. Herbig, W. Ludwig, P. Reischig, E. Lauridsen, T. Marrow, J. Buffière, Non-destructive analysis of micro texture and grain boundary character from x-ray diffraction contrast tomography, *Nuclear Instruments and Methods in Physics Research Section B: Beam Interactions with Materials and Atoms* 268 (2010) 291–296.
- [4] R. Suter, D. Hennessy, C. Xiao, U. Lienert, Forward modeling method for microstructure reconstruction using x-ray diffraction microscopy: Single crystal verification, *Reviews of Scientific Instruments* 77 (2006) 123905 1–12.
- [5] S. Li, R. Suter, Adaptive reconstruction method for three-dimensional orientation imaging, *J. of Appl. Cryst.* 46 (2013) 512–524.
- [6] J. Bernier, R. Suter, A. Rollett, J. Almer, High-energy x-ray diffraction microscopy in materials science, *Annual Review of Materials Research* 50 (2020) 395–436.
- [7] J. Lind, S. Li, R. Pokharel, U. Lienert, A. Rollett, R. Suter, Tensile twin nucleation events coupled to neighboring slip observed in three dimensions, *Acta Materialia* 76 (2014) 213 – 220.
- [8] R. Pokharel, J. Lind, A. Kanjarla, R. Lebensohn, S. Li, P. Kenesei, R. Suter, A. Rollett, Polycrystal plasticity: Comparison between grain-scale observations of deformation and simulations, *Annual Reviews of Condensed Matter Physics* 5 (2014) 317–346.
- [9] R. Pokharel, J. Lind, S. Li, P. Kenesei, R. Lebensohn, R. Suter, A. Rollett, In situ observation of bulk 3d grain evolution during plastic deformation in polycrystalline copper, *Int. J. of Plast.* 67 (2015) 217–2343.
- [10] S. Gustafson, W. Ludwig, P. Shade, D. Naragani, D. Pagan, P. Cook, C. Yildirim, C. Detlefs, M. Sangid, Quantifying microscale drivers for fatigue failure via coupled synchrotron x-ray characterization and simulations, *Nature Communications* 11 (2020) 3189.
- [11] A. King, G. Johnson, D. Engelberg, W. Ludwig, J. Marrow, Observations of intergranular stress corrosion cracking in a grain-mapped polycrystal, *Science* 321 (2008) 382–385.
- [12] J. Hanson, A. Bagri, J. Lind, P. Kenesei, R. Suter, S. Gradecak, M. Demkowicz, Crystallographic character of grain boundaries resistant to hydrogen-assisted fracture in ni-basealloy 725, *Nature Communications* 9 (2018) 3386.
- [13] H. Liu, Y. Zhang, M. J. Wilkin, J.-S. Park, A. D. Rollett, R. M. Suter, 3d in-situ stop action study of recrystallization in additively manufactured 316l stainless steel: Reconstruction optimization and observations,”, 2022. “ accepted for publication in *IOP Conf. Series: Mat. Sci. and Engr.*”.

- [14] C. Hefferan, S. Li, J. Lind, U. Lienert, A. Rollett, R. Suter, Observation of recovery and recrystallization in high purity aluminum measured with forward modeling analysis of high energy diffraction microscopy, *Acta Materialia* 60 (2012) 4311–4318.
- [15] E. Lauridsen, H. Poulsen, S. Nielsen, D. J. Jensen, Recrystallization kinetics of individual bulk grains in 90% cold-rolled aluminium, *Acta Materialia* 51 (2003) 4423–4435.
- [16] A. Bhattacharya, Y. Shen, C. Hefferan, S. Li, J. Lind, R. Suter, C. Krill, G. Rohrer, Grain boundary velocity and curvature are not correlated in Ni polycrystals, *Science* 374 (2021) 189–193.
- [17] A. Bhattacharya, Y.-F. Shen, C. Hefferan, S. Li, J. Lind, R. Suter, G. Rohrer, Three-dimensional observations of grain volume changes during annealing of polycrystalline nickel, *Acta Materialia* 167 (2019) 40–50.
- [18] Y.-F. Shen, S. Maddali, D. Menasche, A. Bhattacharya, G. Rohrer, R. Suter, The importance of outliers: A three dimensional study of grain growth in α -phase iron,, *Phys. Rev. Materials* 3 (2019) 063611.
- [19] J. Zhang, W. Ludwig, Y. Zhang, H. H. B. Sørensen, D. J. Rowenhorst, A. Yamanaka, P. W. Voorhees, H. F. Poulsen, Grain boundary mobilities in polycrystals, *Acta Materialia* 191 (2020) 211–220.
- [20] M. Higgins, J. Kang, G. Huang, D. Montiel, N. Lu, H. Liu, Y. Shen, P. Staublin, J.-S. Park, J. Almer, P. Kenesei, P. Sanders, R. Suter, K. Thornton, A. Shahani, Anomalous strain-energy-driven macroscale translation of grains during nonisothermal annealing, *Physical Review Materials* 5 (2021) L070401.
- [21] C. Zhang, A. Acharya, On the relevance of generalized disclinations in defect mechanics, *Journal of the Mechanics and Physics of Solids* 119 (2018) 188–223.
- [22] C. Zhang, A. Acharya, S. Puri, Finite element approximation of the fields of bulk and interfacial line defects, *Journal of the Mechanics and Physics of Solids* 114 (2018) 258–302.
- [23] C. Fressengeas, X. Sun, On the theory of dislocation and generalized disclination fields and its application to straight and stepped symmetrical tilt boundaries, *Journal of the Mechanics and Physics of Solids* 143 (2020) 104092.
- [24] X. Sun, C. Fressengeas, V. Taupin, P. Cordier, N. Combe, Disconnections, dislocations and generalized disclinations in grain boundary ledges, *International Journal of Plasticity* 104 (2018) 134–146.
- [25] D. Naragani, P. Shade, W. Musinski, D. Boyce, M. Obstalecki, D. Pagan, J. Bernier, A. Beaudoin, Interpretation of intragranular strain fields in high-energy synchrotron x-ray experiments via finite element simulations and analysis of incompatible deformation, *Materials & Design* 210 (2021) 110053.
- [26] R. Pokharel, D. Brown, B. Clausen, D. Byler, T. Ickes, K. McClellan, R. Suter, P. Kenesei, Non-destructive characterization of UO_{2+x} nuclear fuels, *Microcopy Today* 25 (2017) 42–47.
- [27] S. Li, J. Lind, C. Hefferan, R. Pokharel, U. Lienert, A. Rollett, R. Suter, Three dimensional plastic response in polycrystalline copper via near-field high energy x-ray diffraction microscopy, *J. Appl. Cryst.* 45 (2012) 1098–1108.
- [28] Y. Shen, H. Liu, R. Suter, Voxel-based strain tensors from near-field high energy diffraction microscopy, *Current Opinion in Solid State & Materials Science* 24 (2020) 100852 1–8.
- [29] H. Liu, 2022. H. Liu and Y. Zhang and M. Wilkin and J.S. Park and P. Kenesei and A.D. Rollett and R.M. Suter, “3D In-situ Stop Action Study of Recrystallization in Additively Manufactured 316L Stainless Steel: Reconstruction Optimization and Observations,” submitted, 2022.
- [30] D. Menasche, P. Shade, R. Suter, Accuracy and precision of near-field hedm forward-model based microstructure reconstructions, *Journal of Applied Crystallography* 53 (2020) 107–116.
- [31] J. Lind, A. Rollett, R. Pokharel, C. Hefferan, S. Li, R. S. U. Lienert, Image processing in experiments on, and simulations of, plastic deformation of polycrystals, in: *IEEE International Conference on Image Processing (ICIP), IEEE International Conference Image Processing*, 2014, pp. 4877–4881.

- [32] K. E. Nygren, D. C. Pagan, J. V. Bernier, M. P. Miller, An algorithm for resolving intragranular orientation fields using coupled far-field and near-field high energy x-ray diffraction microscopy, *Materials Characterization* 165 (2020) 110366.
- [33] P. Reischig, W. Ludwig, Three-dimensional reconstruction of intragranular strain and orientation in polycrystals by near-field x-ray diffraction, *Current Opinion in Solid State & Materials Science* 14 (2020).
- [34] J. Lind, In-situ High-Energy Diffraction Microscopy Study of Zirconium Under Uni-axial Tensile Deformation, Phd thesis, Carnegie Mellon University, 2013.
- [35] R. Arora, A. Acharya, A unification of finite deformation j2 von-mises plasticity and quantitative dislocation mechanics, *Journal of the Mechanics and Physics of Solids* 143 (2020) 104050.
- [36] R. Arora, X. Zhang, A. Acharya, Finite element approximation of finite deformation dislocation mechanics, *Computer Methods in Applied Mechanics and Engineering* 367 (2020) 113076.
- [37] R. Arora, A. Acharya, Dislocation pattern formation in finite deformation crystal plasticity, *International Journal of Solids and Structures* 184 (2020) 114–135. *Physics and Mechanics of Random Structures: From Morphology to Material Properties*.
- [38] A. Ulvestad, A. Singer, J. Clark, H. Cho, J. Kim, R. Harder, J. Maser, Y. Meng, O. G. Shpyrko, Topological defect dynamics in operando battery nanoparticles, *Science* 348 (2015) 1344–1347.